Improved detectability and signal strength for rotating phase fluorescence immunoassays through image processing

Prasun Mahanti,* Thomas Taylor,* Mark A. Hayes,* Douglas Cochran and Matthew M. Petkus

Received 19th July 2010, Accepted 9th October 2010
DOI: 10.1039/c0an00549e

Fluorescence immunoassays based on rotating solid phase have shown promise of lowered detection limits, among other advantages. However, intrinsic background distortion effects have limited their utility. Here, novel image processing strategies are used to minimize these effects and improve the estimate of concentration and lower the detection limit. This initial demonstration of a new processing capability is performed on data for a protein, myoglobin, which is a biomarker for acute myocardial infarction. For these data, compared with published results, the detection limit is improved by a factor of approximately one hundred (to 700 fM), which is competitive with or better than other immunoassay strategies (ELISA, for example) that are fully developed. This work suggests that image and video processing technologies can provide a valuable alternative approach to biochemical detection and concentration estimation.

Introduction

Automated image analysis is an important tool that finds application in numerous fields in experimental science and medicine. Starting from a known or unknown model of the imaging process and guided by underlying science, image analysis aims at defining a logical, repeatable procedure for harnessing detailed information from an experimental image acquisition system. Epi-fluorescence microscopy applied to fluorescence immunoassays is not an exception, and in this work we show an existing experimental paradigm is significantly improved by image processing for biochemical concentration estimation. A completely automated and novel image processing algorithm was developed to address both image and temporal domain issues.

The biomolecule that we demonstrate this capability on is myoglobin, which is a known acute myocardial infarction (AMI) biomarker. Currently, the electrocardiogram, not biomarkers, is the most commonly used AMI diagnostic. Unfortunately, the results may be subtle and open to interpretation, leading to inconsistent diagnosis, as the sensitivity for AMI is as low as 60%.[1] However, biomarkers are becoming more prominent in analysis; several have been identified as being released into the blood during an AMI event. The current consensus focuses on creatine kinase, troponins, C-reactive protein, and myoglobin.[2–4] Of the four, myoglobin is released earliest into the bloodstream, making it the best candidate marker for early diagnosis.[3,5,6] The choice of AMI biomarker(s) for best practices is still in flux though.[7–14] Assessment of commercial tests for myoglobin, and related biomarkers indicates detection limits in the 0.2 ng mL^{-1} (0.5 pM) range.[6,57–59]

A very large number of fluorescence immunoassays currently exist for detecting specific biomolecular targets providing a concentration estimation.[15–17] Starting with Coons in 1941,[18] fluorescence and related techniques have bloomed into a myriad of applications (most recent ones referenced[19–21]) and systems. Related strategies currently of interest include plasmon-enhanced systems,[7–9,22,23] the associated areas of energy transfer, polarization, and quenching,[24–31] lifetime/time resolved,[32,33] enhanced fluorescence (including quantum dots)[34–36] and flow/micro/bead augmented.[37–39] All of these systems adhere to a few general approaches to immunoassay, including 1) direct assays, where the antigen target is labeled, 2) sandwich assay, where the antigen binds two antibodies, one of which is labeled, and 3) competitive assays, where a labeled antigen competes with the binding site, thus influencing the signal.[17]

The approach here relies on rotating solid surface self assembled from paramagnetic particles[40] to both generate convective mixing and encode the optical signal (Fig. 1).[41–44] Recently, this technique has been used to target proteins (myoglobin) and previously, for small molecules (cortisol, potential adrenalin secretion indicator) demonstrating that a sensitive assay can be performed. However, this method, which clusters the signal part from the unbound analyte and incorporates a time-variability into the signal, also dynamically changes the combined effect of background fluorescence and illumination non- homogeneity. In standard procedures methods such as 'flat-fielding' from initial conditions often help in eliminating distortions,[45] but in the case of the rotating solid phase immunoassay, such methods were found to offer no improvements.

This approach is differentiated from ELISA in that the signal is maintained at the surface, which allows for amplification *via* isolation and manipulation of the surface (formation of rotors and their movement) coupled with image processing–compared with amplifying the signal through enzymatic reaction and release to bulk solution. These are fundamentally different approaches, where detection limits of the new strategy are already comparable to techniques that have been developed for decades (hovering around 0.5 pM). The surface localization is especially useful from the image processing standpoint, as distinct signal objects are easier to detect and quantify, and

Arizona State University, Tempe, Arizona. E-mail: mhayes@asu.edu

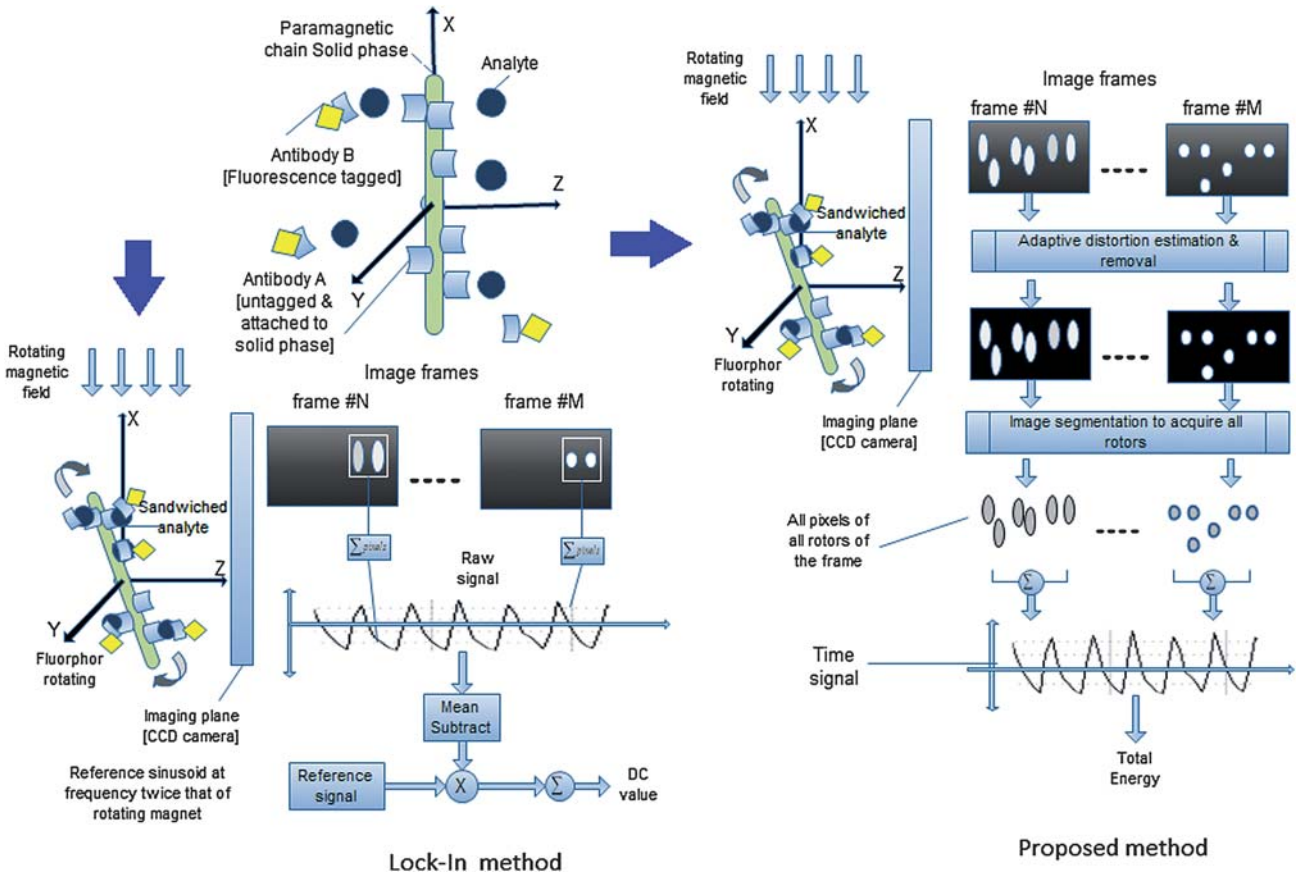

Fig. 1 Paramagnetic chain solid phase (top-left) rotates in magnetic field and images are acquired by CCD camera identically for both the lock-in (bottom-left) and the proposed method (right). The sandwiched analyte and the fluorescence tag rotate with the paramagnetic chain and appear as rotating blobs (rotors) in the image frames. In the lock-in method, some of these rotors are manually cropped by selecting a rectangular region including the rotors. In the proposed method, all of the rotors are automatically segmented (optimal selection of pixels that belong to rotors). The proposed method also has a distortion correction block which plays the main role in reducing the signal variability at each concentration of the analyte.

because they are not spread over the entire field-of-view, the effective spatial noise is minimized.

To begin to improve the assay, the various factors influencing signal-to-noise ratio were considered.[46–53] Among these, background fluorescence is considered a severe hindrance for fluorescence immunoassays[54] and combating its effects is a serious concern in clinical tests such as ELISA.[55] This initial assessment led to the identification and resolution of the most important problem in the existing method,[41] which is the spatio-temporal variable background fluorescence and distortion. The images acquired from epi-fluorescence microscopy represent the fluorescent signal in 2-d, which is then converted into a 1-d function. While selecting the correct mathematical transformation (image-to-time series) is very important, the initial concern is the efficient acquisition of the signal in the 2-d (image domain). Effective signal analysis near or at the detection limit (by definition) is restricted by confounding effects, including the background noise from unbound analyte and the environment.

A novel algorithm which dynamically recreates the background and distortion effects for each frame is used to address the complex background (algorithmic details of the distortion field estimation may be found in here[56]). Image acquisition defects are then identified, estimated, and normalized, which effectively minimizes or eliminates (undetectable) the background and distortion effects, resulting image frames that contain strong signal clusters in minimum CCD noise. Image processing algorithms segment these regions and use the intensity values of the corresponding pixels to generate a one dimensional time-series. Taking into account that all modes of frequency excitation contribute to the signal energy, the averaged signal energy is used to estimate concentration. This reduces the detection limits and extends the dynamic range for the demonstration biomarker target and suggests that this strategy can be extended to other dynamic imaging systems, including other biomarkers.

Experimental

Because the focus of this work is on the improvement of the analysis phase rather than the experimental, we confine our description to modulated sandwich assays. Details of the experimental procedure have been covered in earlier literature, where the important portions are reiterated here that directly impact the data generation process. Conceptual comparison of the lock-in method and the proposed method is shown in Fig. 1. In broad terms, the magnetic microparticles (BioMag, 1.6 μm average diameter, Qiagen, Inc., Valencia, CA) were coated with the myoglobin antibody, exposed to the analyte at the

appropriate concentration, rinsed, then exposed to the secondary antibody. They were then placed on a microscope slide, the rotating magnetic field was applied, and the image collected.[41,44] Supraparticle structures with the approximate dimensions ranging from 50 to 100 μm lengths, 5–10 μm widths, and 8–15 μm thicknesses was observed.[40,41,43]

Protein preparation and data collection

Two milligrams of lyophilized cardiac equine myoglobin (MW 16 950, Sigma, St. Louis, MO) was dissolved into a 1.5 mL volume centrifuge tube containing 1 mL of 100 mM carbonate buffer, free of sodium azide at a pH of 8.5. One milligram of fluorescein-5-EX, succinimidyl ester (FEXS, Invitrogen, Carlsbad, California) was dissolved into a 0.5 mL-volume centrifuge tube containing 0.1 mL of DMSO (Sigma, St. Louis, MO). The FEXS solution was immediately added dropwise to the myoglobin solution at room temperature. This was allowed to react for an hour in darkness at room temperature on a Vortex Genie-2 (VWR Scientific, West Chester, PA). The crude reaction mixture was placed into a dialysis membrane with a cut-off value of 1 kD (Sigma, St. Louis, MO). The mixture was dialyzed against 5 exchanges of 1 L of 100 mM phosphate buffered saline (PBS) at a pH of 7.4 with 0.1% sodium azide (Sigma, St. Louis, MO). The solution outside of the membrane was monitored spectroscopically for fluorescence to ensure that dialysis was complete. A 1 mL aliquot of polyclonal goat anti-equine myoglobin (Pab, Immunology Consultants Laboratory, Inc., Newberg, OR), 1 mg mL^{-1}, was initially dialyzed to remove existing sodium azide preservative. The Pab was then reacted in the same manner as cardiac equine myoglobin.

Dialyzed FEXS-myoglobin and FEXS-Pab were analyzed by absorbance measurements (U-2000 spectrophotometer, Hitachi, Tokyo, Japan). From these measurements, it was determined that 1–2 FEXS molecules were conjugated to a single myoglobin molecule and ~20 FEXS molecules were conjugated to a single Pab molecule. It is noted that a lower degree of labeling on the Pab could be accomplished in the future by dialysis followed by exchange or desalting column. The proteins were then stored at 4 °C until used.

Assay solutions were made using 30 mL of the Pab-particle colloid combined with 30 mL of unlabeled cardiac myoglobin concentrations. These buffer solutions were incubated for 1 h on a Vortex Genie-2. FEXS-Pab stock solution (1 mL) was added to each solution and allowed to incubate for an additional hour on the Vortex Genie-2 followed by 10 washes with PBS buffer.

An Olympus I - 70 inverted microscope (Tokyo, Japan) with a charge coupled device (CCD) camera connected to a computer with image-capture capability (QICAM Fast 1394, QImaging, Burnaby, Canada).[41,44] Multiple 15 mL-sized droplets were analyzed for each assay solution using a microscope slide with a concavity (LabScientific, Livingston, NJ). A cylindrical rare earth magnet (2.75 cm diameter, 0.25 cm thick) was used to generate the magnetic field (Edmund Scientific, NY). The magnet was mounted to a 7 cm-long rod connected to a DC motor controlled *via* a custom-designed circuit. For the modulated structure assay, the magnet was rotated at a constant frequency, typically at 1.5 Hz. Illumination from a mercury lamp was passed through the appropriate filter cube and a 40× objective to excite the assay solution. Emitted fluorescence was collected with the CCD and stored as video. The images (348 × 260 pixels) were captured at an exposure time of ~50 ms (gain, 2000; offset, 2600) which translates to a rate of ~20 frames s^{-1}.

The image sequence analysis involves three different stages. The data acquisition process uses a CCD camera which images an object in solution through an array of optics. Moreover, the object is in a solution in which the lighting conditions are influenced by the excess of fluorescence particles as well as the object itself. These lead to a number of distortions in the acquired image where the combined effects are captured in a distortion model. In the first stage, the image sequence is preprocessed for distortion correction. After the image has been normalized for distortion, the image is segmented into signal objects of interest and the background areas. The segmentation is accomplished in the second stage, at the end of which, for each frame of the video acquired, we precisely know which pixels are to be considered for signal extraction. The selected pixels have a very high signal to noise ratio when compared to the 'zero' concentration data.

The final step accumulates the signal information from all the selected pixels in each frame. The result is the formation of a 1-dimenstional time series which directly correlates with the fluorescence signal intensity across the image frame sequence. The average energy of the signal for fixed (128) number of frames is used to generate the signal-concentration curve.

Image processing

A brief description of the algorithms in the image processing blocks mentioned above is provided next. However, a highly detailed description can also be found.[56,60]

A Pre-processing. The pre-processing block corrects the image distortion error. The distortion that is captured in the image is modeled as spatial product and additive term. The multiplicative effects are mostly spatial, and the additive effects are mostly temporal for an image sequence. The image distortion of an image ($I_0(x,y)$) is modeled as

$$I(x,y) = I_0(x,y)\cdot R_1(x,y) + R_2(x,y) \quad (1)$$

where $R_1(x,y)$ is the multiplicative distortion effect, $R_2(x,y)$ is an additive distortion effect and $I(x,y)$ is the distorted image. It may be noted that the multiplicative distortion is mostly due to uneven illumination while the additive distortion is mostly due to electronic bias and noise. The above model suggests the following distortion correction model:

$$I_0(x,y) = \frac{I(x,y) - R_2(x,y)}{R_1(x,y)} \quad (2)$$

We choose to determine the multiplicative spatial component adaptively for each frame assuming the additive component to be small magnitude of uncorrelated noise. To estimate R_1, we use surface fitting among the well-known methods for shading correction.[61,62] A novel method of estimating a smooth surface by a stack of quadratic curves is employed for estimating the distortion in the least square error sense. Hence, after estimating R_1, our modified image correction model becomes

$$I_0(x,y) \cong \frac{I(x,y)}{R_1(x,y)} \quad (3)$$

The estimated distortion is utilized to normalize it, giving us the image ready for segmentation.

B Image segmentation. The image segmentation block extracts the pixels that primarily reflect rotor fluorescence intensity. The rotor pixel intensities are higher than the now-normalized background; therefore, a global thresholding is employed using a minimum error thresholding algorithm.[63] However, to preserve all the signal pixels, a 'guard-band' is used around the segmented rotors. This process generates a binary mask $F(x,y)$ indicating the spatial position of the pixels that should be selected. The intersection of the image and the binary mask directly gives us the signal pixels $S(x,y)$:

$$S(x,y) = F(x,y) \cap I(x,y) \quad (4)$$

C Time signal analysis. The time signal analysis block first generates the time series from the selected pixels. This is done by a simple summation of intensity values. The 128 time signal points are averaged into a single signal energy quantifier for each time series generated across similar and dissimilar set of concentrations. The average signal energy of a sequence of frame is calculated as

$$E_{S,avg} = \frac{1}{T}\sum [x(n)]^2 \quad (5)$$

where T is the total number of frames and $x(n)$ is the time signal value for the n^{th} frame.

Results and discussion

Image processing provides for improved results because of the recognition and removal of a distortion effect present in the original data, as well as a more complete description of the modulated signal and its method of collection. In this section, the image distortion, its effects, and its correction are described. Next, the temporal signal obtained from the distortion corrected frames is defined, and its assessment leading to the results is explained. Lastly, the current and previous approach results are quantitatively compared.

Modeling and effects of imaging distortion

The image distortion effect is first modeled, its veracity assessed, and strategies for its removal are described.

Modeling. For an illuminated blank image (no rotors, *etc.*), the pixel values would be expected to signify only the instrument noise. However, the actual image looks much different (Fig. 2c), where there is considerable illumination in the center while the sides have much less. The 3-D (or three-dimensional) view of the blank data (Fig. 2e) clearly shows this uneven illumination, where the sides and corners have lower pixel values. This distortion is most likely from inhomogeneous gain of CCD pixels and uneven illumination and can be modeled as spatial product distortions, with additional instrument noise. Thus, our model includes spatially resolved multiplicative component ($R_1(x,y)$) and an additive one ($R_2(x,y)$). With this model, if there is no object within the image, then:

$$\begin{aligned} I_0(x,y) &= 1 \ ; \forall (x,y) \\ I(x,y) &= R_1(x,y) + R_2(x,y) \end{aligned} \quad (6)$$

This vector description captures the essence of the distortion effects in blank images and in the background of data images.

Increase in variance. This distortion is present for all of the frames, is not constant, and dramatically increases the variance. The effects can be trivially assessed by considering a single pixel 'X' in the image frame (discard the position indices), and stating that:

$$\begin{aligned} X &= S + N; \ \mathrm{var}(N) = \sigma^2 \\ X &= R_1 S + R_1 N; \ \mathrm{var}(N) = R_1{}^2\sigma^2 \end{aligned} \quad (7)$$

where S is the signal, N is the noise, and the second equation represents the addition of the distortion effects. The actual scenario is certainly much more complex as the distortion is not fixed, either spatially or temporally across the image sequence. The result of not removing this source of noise is an increase the variability of the lock in output.

Decrease of SNR. The distortion also decreases and skews the signal. To understand the distortion, a signal region is defined as the image of a single rotor (Fig. 3). Image thresholding is performed to designate pixels belonging to signal region based on the pixel intensity. When significant distortion is present, a single global threshold leads to selection of inappropriate regions. Either more pixels would be included which are background pixels and contribute only to the noise (Fig. 3a), or less pixels are included, thus losing signal (Fig. 3b). An optimal procedure should help extract more signal and less background (Fig. 3c). Such a procedure either takes account of the spatial distortion during thresholding or removes it. In the proposed method, we choose to remove the distortion before thresholding.

Introduction of non-linearity to concentration *versus* signal. Even when the local threshold is set appropriately, the distortion induces non-linearity in the concentration-signal relationship. As another trivial example (noting, of course, that real data sets are more complex), consider two representative model image frames (Fig. 4a and 4b) containing distortion at two different concentrations. The total signal strength in first frame (Fig. 4a) is $100 \times 10 + 10 \times 10 = 1100$, while for the second (Fig. 4b), it is $50 \times 10 + 50 \times 20 = 1500$. If we do not include the distortion, then the total signal in first case is 20, and in second case is 100. What appears to be a fractional increase should actually be a 5 times increase. Also, the rotors exhibit translational motion and thus drift from one region of distortion to other.

Clearly this distortion is a true nuisance parameter with detrimental effects in the signal to noise ratio and in estimating the signal-concentration correlation. Removal of this distortion presents a significant opportunity to improve the data processing for this technique, noting it will be necessary to estimate the distortion adaptively for each frame and normalize it by method of division as suggested by the image correction model.

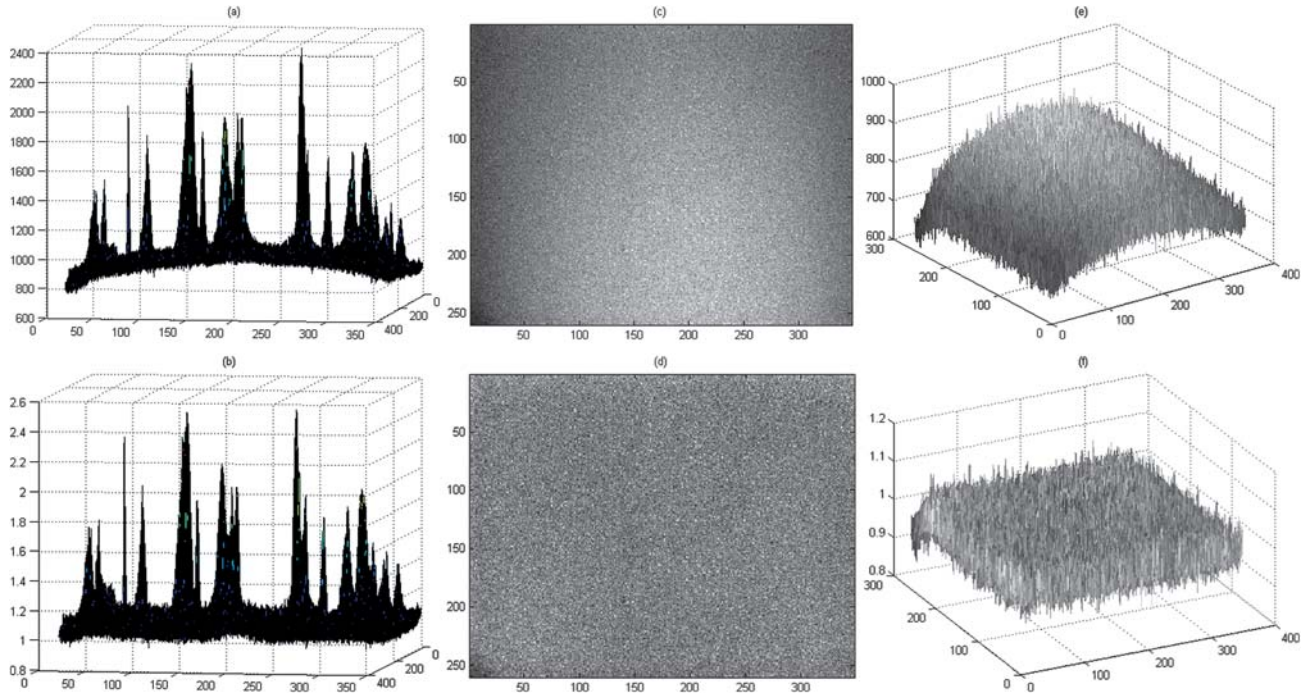

Fig. 2 Effect of distortion and its correction. (a) Normal frames showing distortion causing the base plane to become curved. (b) Effect after distortion removal for normal frames. (c) Empty (control) frame image before distortion removal. (d) Empty frame image after distortion removal. (e) Empty frame image surface before distortion removal. (f) Empty frame image surface after distortion removal.

Image distortion correction

To estimate the distortion (R_1), we use surface fitting to establish the field of shading correction. The control points for distortion surface fitting are selected dynamically; at the same time, a binary matrix F is generated with 1's at pixels which belong to a signal object. A smoothed control frame is used to correct the distortion while accounting for not using the actual distortion surface. The method of creating the surface works by scanning each row or column of the control point matrix sequentially, fitting it to a quadratic function, and stacking the resulting curves in order to calculate the surface. Experiments with 500 pM myoglobin illustrate strategy, showing the original data (Fig. 2a) and distortion-corrected data (Fig. 2b). Simple visual inspection indicates that the noise variance is very small and spatially evenly distributed after correction. This effect is quantified by calculating the variance of each pixel across all the images in a temporal stack prior to and after distortion correction. The variance has been greatly (very greatly, approximately 10^5+) reduced (Fig. 5); the noise mean of the corrected frames vary between 1 and 1.02 across all frames and all concentrations. The noise variance is less than 0.004 for most of the frames. An interesting result of this correction is that the noise is spatially stationary—the same level of noise now exists over all the signal pixels.

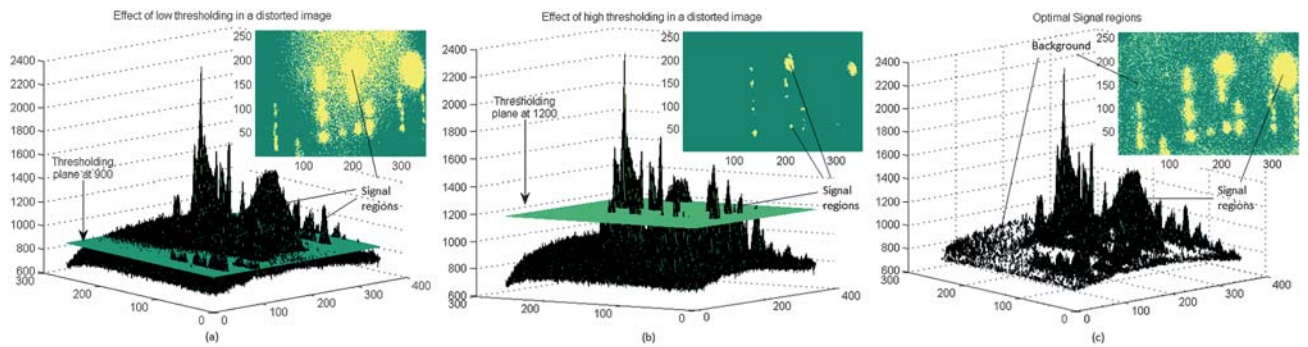

Fig. 3 Signal regions and background noise is shown in three different cases of thresholding a distorted image frame. The distortion can be seen in all the frames as a curvature in the image base plane. In case of low thresholding (a) by a thresholding plane fixed at a pixel intensity value of 900, most of the pixels corresponding to rotors are extracted but a large amount of background pixels are also acquired. The opposite occurs in (b) where the thresholding plane is fixed at an intensity value of 1200. Much less background is acquired but the number of true signal pixels is also reduced. The effect of optimal extraction of signal regions is shown in (c) where the thresholding plane almost merges with the image base plane, thus extracting most of the true signal pixels and less background.

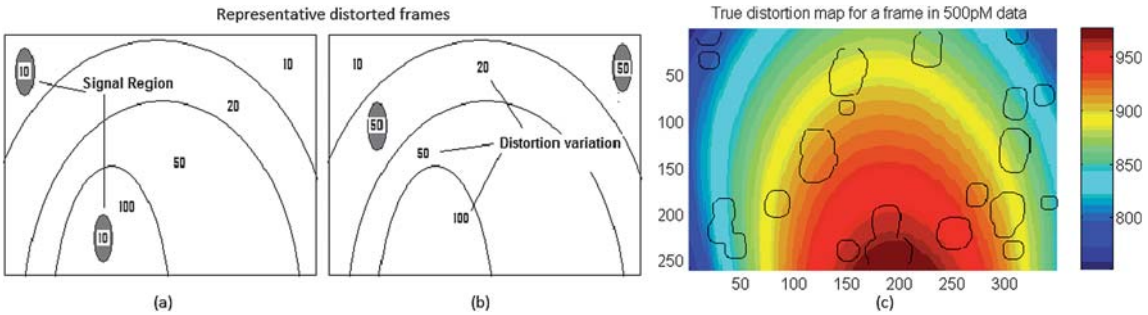

Fig. 4 Representative distorted image frames of different concentrations with rotors at different locations of frame (a–b). The signal regions are shown in gray. A true distortion map extracted from a frame of the 500 pM concentration image sequence (c) shows the similarity with the representative distorted frames. The spatial intensity (pixel value) is color coded in (c).

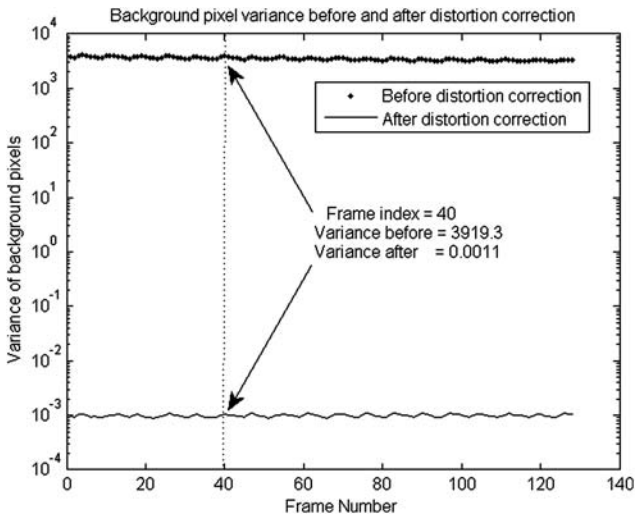

Fig. 5 Variance of background pixels before and after distortion correction. Note the difference in magnitude of variance and logarithmic scale on vertical axis. The variance of background pixels is reduced by a factor of 10^5 approximately.

Signal model and definition

If the surface area of a rod rotating in space is projected to a flat surface, it would vary approximately as a rectified sinusoidal waveform (Fig. 4). The Fourier series of this wave is:

$$f(n) = \frac{2}{\pi} - \frac{4}{\pi}\left[\frac{\cos 2\omega_0 n}{1.3} + \frac{\cos 4\omega_0 n}{3.5} + \frac{\cos 6\omega_0 n}{5.7} + \ldots.\right] \quad (8)$$

This model waveform can provide a tool to begin to understand the advances associated with this new approach. The lock-in method successfully extracts the power of the first sinusoidal term (a small portion of the total signal power), where the frequency is twice that of the magnet rotation, but does not capture the remaining terms. Beyond this idealistic description, the real signal is neither a simple sinusoidal nor a full-wave rectified waveform; it is a combination of a number of rectified time signals—the rectification being a direct result of the projection. Furthermore, the combination of many individual structures contributing and the non-rigid nature of the structures dampens the signal compared to the ideal form.

Pixel identification. The current approach attempts to define signal-containing pixels (on a frame by frame basis), compared to the previous method where a global 150 × 120 pixel box was used to define a data set with two signal objects present. First, due to the fixed size of the box and the signal region never occupying more than 30% of the total number of pixels, a large number of noise pixels were included increasing the noise power. Second, the total data stream contained approximately 10 to 15 rotors of different sizes. By capturing only two of them, a large part of the signal power is lost. Both these negative effects are countered by effective image segmentation. We currently use multiple rods within our image. While the variance among different rotors in the same image frame is of abstract scientific interest, our current focus is to determine only the total effect of all the bound analyte. Thus, in this work, we pool all of the effective signal pixels together irrespective of originating signal object.

Temporal signal assessment

The signal represents the change in fluorescent intensity which varies with time across the image sequence. To begin to assess the temporal pattern of intensity, all signal-containing pixels (defined by threshold strategy) are summed for each frame, and this scalar value represents a single point in the temporal sequence. Let a single frame contain "K" signal regions, and let the signal region pixel intensities be denoted as "s". Then, if R_i denotes a signal region, the time signal value for the n^{th} frame can be written as:

$$x(n) = \sum_{R_1} s + \sum_{R_2} s + \ldots\ldots\ldots \sum_{R_K} s \quad (9)$$

The temporal signal (Fig. 6) can be seen to be nearly periodic and contains multiple harmonics. Also, the signal is time-varying, and its period varies from 6 to 10 frames. The signal energy (E_s) per frame is the square of total intensity of the frame:

$$E_{S,frame} = [x(n)]^2 \quad (10)$$

and the average signal energy of a sequence of frames is calculated with eqn (5).

In the case where there are signal objects in motion, the signal power is found for a sequence of frames. The signal-to-noise power ratio is defined as the average signal energy per frame compared to the average noise energy per frame.

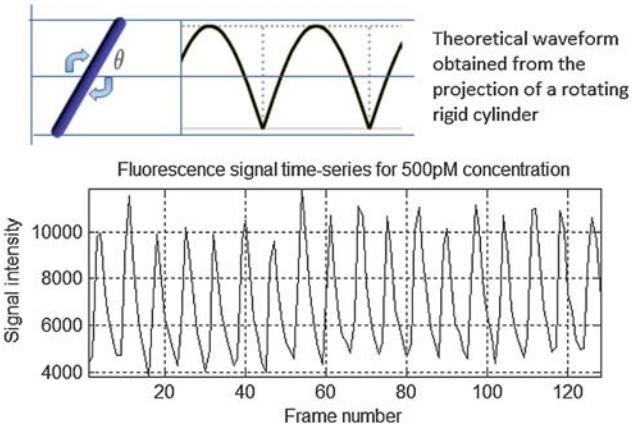

Fig. 6 Theoretical waveform from a rigid rotating cylinder (top) is compared to the actual time signal obtained from an image sequence (bottom). The true signal appears to look similar but is highly complex and composite as the rotating chains are not rigid, do not have length or shape similarity, and are numerous. A very small fraction of the actual signal strength is captured by a model assuming a pure sinusoid behavior as in lock-in.

Quantification of improved metrics

The quantification is based upon the change in intensity assigned as signal when the concentration is altered. By removing the distortion from the images, defining signal pixels in each frame, and calculating the temporal total signal, a dramatic improvement in signal-to-noise levels and detection limit is generated. We use the signal energy as the metric for the quantification of signal strength (Fig. 7, Table 1). The figures of merit were calculated identically for each strategy, where the detection limit is estimated as two times the standard deviation at zero concentration compared to the slope at low concentrations.

For this direct comparison (Fig. 7, Table 1), the mean signal power from the image processing method is more than 30 dB (1000 times) higher for all signal concentrations and the variability is greatly reduced. The combination of reduced variance (the largest factor) and increased intensity resulted in the detection limit improving by 100 times; for lock-in, the reported detection limit was 70 pM and for the current method, is approximately as low as 700 fM. The dynamic range for the proposed method is 0.68 pM to approximately 2 nM, compared to the lock-in method which is 70 pM to 2 nM. The proposed method shows much higher slope at lower concentrations than the lock-in method (about 60 times greater). The change in sensitivity is largely due to the reduction in spatial variance which enhances the difference between stray signal at zero concentration and the real signal at concentrations higher than 0.68 pM. Also, the lock-in method described in the earlier strategy[13] takes 10 min of analysis time after incubation, while the proposed method takes less than a minute. The reduction is mostly due to the fact that the lock-in method requires a user to manually select the rotors in every frame of a sequence while the proposed method achieves this automatically. The data for the lock-in are the calculated values reported in an earlier study.

Table 1 Numerical comparison of figures of merit

	Limit of detection	Dynamic range (10^x)
Lock-in	70 pM	1.5
Proposed method	0.68 pM	3.5
Factor of improvement	103	2.33

From the plot of the standard deviation of the signal power, the two methods appear to generate opposing trends (Fig. 7, right graph). There is an inherent difference in the signal collection for the two methods. For the lock-in, it is the total brightness captured in a fixed-size window. At lower concentrations, there are more dark pixels. When the lower concentrations are coupled with the product-type distortion, which is when the intensity pixels on the rotors contribute both at the periphery of the image (where there is higher spatial distortion) and at the center (where the distortion is less), large variations in

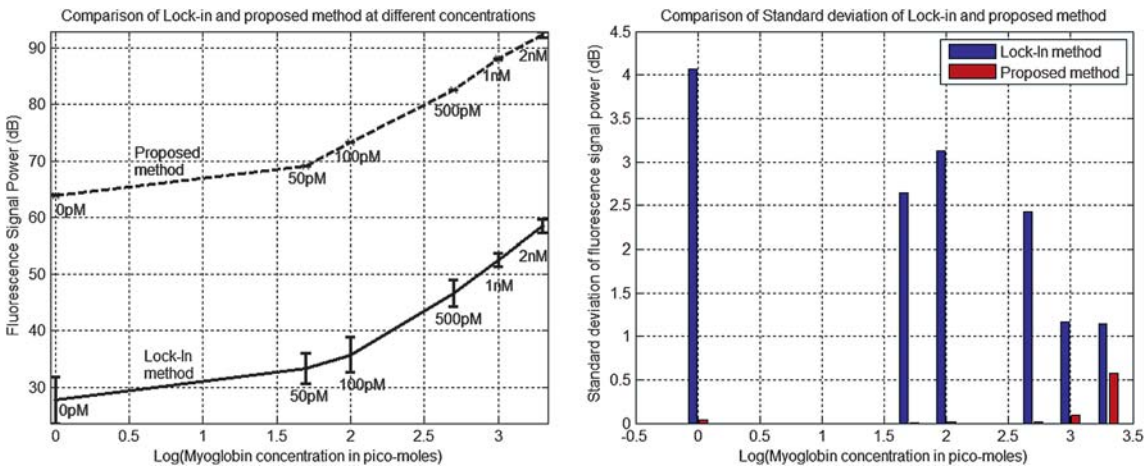

Fig. 7 Signal strength at different concentrations for the proposed method and lock-in approach is compared in (a). The curve from the proposed method is about 30 dB higher than the curve of lock-in. Error bars are present for both curves but are very small and not visible in case of the proposed method. The error bars are compared separately in (b). The same experimental data (image sequences) is used for the comparison. In these data, three different droplets have been examined for each concentration, placed on a slide and data captured.

the average brightness occur across the image plane. As concentration increases, more and more of this fixed-size window gets covered (due to larger signal regions). Accordingly, more and more of the distortion is averaged at each image frame, and the variation decreases among the means of these frames.

In the case of our image processing method, the signal has been corrected for distortion (but not noise), and each pixel selected by image thresholding has a non-zero-mean noise. The sum of all such pixels contributes to the signal power, and the noise contributes to the variability. At higher concentrations, more pixels are used, and the standard deviation increases correspondingly. At very high concentrations (1 nM and 2 nM), the range of the detector is exceeded, and high signal regions were found to be saturated, which introduces some amount of non-linearity for both of the methods. In fact, for the lock-in method, we find that at the two highest concentrations, the variation is almost constant.

Conclusion

The algorithm proposed in this work improves the figures of merit of the lock-in method by a significant amount. The image analysis algorithm is robust and takes only a fraction of the analysis time compared to the lock-in method as it does not require user interaction. The experimental set-up is simple, economical, and has a built-in potential for parallel immunoassay analysis. The improvements point to a newer direction of fluorescence immunoassays conducted with a rotating phase and analyzed by image processing techniques. This new direction can lead to a sensitive and fast alternate diagnostic technique for AMI patients.

Acknowledgements

This work was supported in part with NIH grants 2RO1EB004761-06 and R21EB010191-01A1.

References

1 H. S. Lee, S. J. Cross, P. Garthwaite, A. Dickie, I. Ross, S. Walton and K. Jennings, *Heart*, 1994, **71**, 311–315.
2 M. Kemp, J. Donovan, H. Higham and J. Hooper, *Br. J. Anaesth.*, 2004, **93**, 63–73.
3 A. H. B. Wu, F. S. Apple, W. B. Gibler, R. L. Jesse, M. M. Warshaw and R. Valdes, *Clin. Chem.*, 1999, **45**, 1104–1121.
4 R. J. Dewinter, R. W. Koster, A. Sturk and G. T. Sanders, *Circulation*, 1995, **92**, 3401–3407.
5 R. J. de Winter, J. G. Lijmer, R. W. Koster, R. J. Hoek and G. T. Sanders, *Ann. Emerg. Med.*, 2000, **35**, 113–120.
6 C. Montague and T. Kircher, *Am. J. Clin. Pathol.*, 1995, **104**, 472–476.
7 J. N. Anker, W. P. Hall, O. Lyandres, N. C. Shah, J. Zhao and R. P. Van Duyne, *Nat. Mater.*, 2008, **7**, 442–453.
8 E. Delamarche, G. Sundarababu, H. Biebuyck, B. Michel, C. Gerber, H. Sigrist, H. Wolf, H. Ringsdorf, N. Xanthopoulos and H. J. Mathieu, *Langmuir*, 1996, **12**, 1997–2006.
9 J. C. Riboh, A. J. Haes, A. D. McFarland, C. R. Yonzon and R. P. Van Duyne, *J. Phys. Chem. B*, 2003, **107**, 1772–1780.
10 K. Aslan and C. D. Geddes, *Plasmonics*, 2006, **1**, 53–59.
11 E. Matveeva, Z. Gryczynski, I. Gryczynski, J. Malicka and J. R. Lakowicz, *Anal. Chem.*, 2004, **76**, 6287–6292.
12 E. G. Matveeva, Z. Gryczynski and J. R. Lakowicz, *J. Immunol. Methods*, 2005, **302**, 26–35.
13 L. Piras and S. Reho, *Sens. Actuators, B*, 2005, **111–112**, 450–454.
14 S. Johnston, R. Brightwell and M. Ziman, *Emerg. Med. J.*, 2006, **23**, 331–334.
15 Edwards, R., Ed. *Immunoassays Essential Data*; John Wiley & Sons: Chichester UK, 1996.
16 J. M. VanEmon. *Immunoassay and other bioanalytical techniques*; Boca Raton: CRC Press/Taylor & Francis, 2007.
17 Wild, D., Ed. *The Immunoassay Book*, 3rd ed.; Elsevier: Amsterdam, 2005.
18 A. H. Coons, H. J. Creech and R. N. Jones, *Proceedings of the Society for Experimental Biology and Medicine*, 1941, **47**, 200–202.
19 E. K. Park, W. C. Jung and H. J. Lee, *Acta Vet. Hung.*, 2010, **58**, 83–89.
20 P. T. Charles, A. A. Adams, P. B. Howell, S. A. Trammell, J. R. Deschamps and A. W. Kusterbeck, *Sensors*, 2010, **10**, 876–889.
21 S. H. Zhong, F. P. Qi and M. C. Xu, *Chemia Analityczna*, 2009, **54**, 827–839.
22 H. P. Song, S. Ritz, W. Knoll and E. K. Sinner, *J. Struct. Biol.*, 2009, **168**, 117–124.
23 R. Luchowski, E. G. Matveeva, T. Shtoyko, P. Sarkar, L. D. Patsenker, O. P. Klochko, E. A. Terpetschnig, J. Borejdo, I. Akopova, Z. Gryczynski and I. Gryczynski, *Curr. Pharm. Biotechnol.*, 2010, **11**, 96–102.
24 W. Dandliker and G. A. Feigen, *Biochem. Biophys. Res. Commun.*, 1961, **5**, 299.
25 E. J. Shaw, R. A. A. Watson, J. Landon and D. S. Smith, *J. Clin. Pathol.*, 1977, **30**, 526–531.
26 P. L. Khanna and E. F. Ullman, *Anal. Biochem.*, 1980, **108**, 156–161.
27 G. Khoschsorur, F. Fruehwirth, S. Zelzer, M. Stettin and G. Halwachs-Baumann, *Clin. Chim. Acta*, 2007, **380**, 217–221.
28 D. S. Smith and S. A. Eremin, *Anal. Bioanal. Chem.*, 2008, **391**, 1499–1507.
29 L. Z. Liu, X. H. Dong, W. L. Lian, X. N. Peng, Z. H. Liu, Z. K. He and Q. Q. Wang, *Anal. Chem.*, 2010, **82**, 1381–1388.
30 Y. Ohiro, H. Ueda, N. Shibata and T. Nagamune, *J. Biosci. Bioeng.*, 2010, **109**, 15–19.
31 C. X. Tan, N. Gajovic-Eichelmann, W. F. M. Stocklein, R. Polzius and F. F. Bier, *Anal. Chim. Acta*, 2010, **658**, 187–192.
32 L. Sironi, S. Freddi, L. D'Alfonso, M. Collini, T. Gorletta, S. Soddu and G. Chirico, *J. Biomed. Nanotechnol.*, 2009, **5**, 683–691.
33 H. F. Jiang, G. L. Wang, W. Z. Zhang, X. Y. Liu, Z. Q. Ye, D. Y. Jin, J. L. Yuan and Z. G. Liu, *J. Fluoresc.*, 2010, **20**, 321–328.
34 X. S. Zhu, D. Y. Duan and N. G. Publicover, *Analyst*, 2010, **135**, 381–389.
35 R. Nooney, A. Clifford, X. LeGuevel, O. Stranik, C. McDonagh and B. D. MacCraith, *Anal. Bioanal. Chem.*, 2010, **396**, 1127–1134.
36 Y. X. Zhang, A. Dragan and C. D. Geddes, *J. Appl. Phys.*, 2010, **107**, DOI: 10.1063/1.3284081.
37 F. Lacharme, C. Vandevyver and M. A. M. Gijs, *Microfluid. Nanofluid.*, 2009, **7**, 479–487.
38 S. A. Peyman, A. Iles and N. Pamme, *Lab Chip*, 2009, **9**, 3110–3117.
39 R. S. Sista, A. E. Eckhardt, V. Srinivasan, M. G. Pollack, S. Palanki and V. K. Pamula, *Lab Chip*, 2008, **8**, 2188–2196.
40 M. A. Hayes, N. A. Polson and A. A. Garcia, *Langmuir*, 2001, **17**, 2866–2871.
41 M. M. Petkus, M. McLauchlin, A. K. Vuppu, L. Rios, A. A. Garcia and M. A. Hayes, *Anal. Chem.*, 2006, **78**, 1405–1411.
42 A. K. Vuppu, A. A. Garcia, M. A. Hayes, K. Booksh, P. E. Phelan, R. Calhoun and S. K. Saha, *J. Appl. Phys.*, 2004, **96**, 6831–6838.
43 M. A. Hayes, N. A. Polson, A. N. Phayre and A. A. Garcia, *Anal. Chem.*, 2001, **73**, 5896–5902.
44 M. A. Hayes, M. M. Petkus, A. A. Garcia, T. Taylor and P. Mahanti, *Analyst*, 2009, **134**, 533–541.
45 M. Seul; L. OGorman; M. J. Sammon. *Practical Algorithms for Image Analysis: Descriptions, Examples, and Code*, 2nd ed.; Cambridge University Press: NY NY, 2000.
46 E. P. Kartalov, J. F. Zhong, A. Scherer, S. R. Quake, C. R. Taylor and W. F. Anderson, *BioTechniques*, 2006, **40**, 85–90.
47 P. R. Knight, A. Sreekumar, J. Siddiqui, B. Laxman, S. Copeland, A. Chinnaiyan and D. G. Remick, *Shock*, 2004, **21**, 26–30.
48 K. K. Sin, C. P. Y. Chan, T. H. Pang, M. Seydack and R. Renneberg, *Anal. Bioanal. Chem.*, 2006, **384**, 638–644.
49 K. Kuwabara, M. Ogino, T. Ando and A. Miyauchi, *Appl. Phys. Lett.*, 2008, **93**, DOI: 10.1063/1.2960354.
50 T. Shtoyko, E. G. Matveeva, I. F. Chang, Z. Gryczynski, E. Goldys and I. Gryczynski, *Anal. Chem.*, 2008, **80**, 1962–1966.

51 D. R. Smith, C. A. Rossi, T. M. Kijek, E. A. Henchal and G. V. Ludwig, *Clinical And Diagnostic Laboratory Immunology*, 2001, **8**, 1070–1075.
52 L. M. Lei, Y. S. Wu, N. Q. Gan and L. R. Song, *Clin. Chim. Acta*, 2004, **348**, 177–180.
53 H. J. Kim, W. L. Shelver, E. C. Hwang, T. Xu and Q. X. Li, *Anal. Chim. Acta*, 2006, **571**, 66–73.
54 H. Schneckenburger, B. W. Reuter and S. M. Schoberth, *Trends Biotechnol.*, 1985, **3**, 257–261.
55 J. Gibbs. *Selecting the detection system – colorimentric, fluorescent, luminiscent methods (ELISA technical bulletin no 5)*. Corning Incorporated: Life Sciences 2001, http://catalog2.corning.com/Lifesciences/media/pdf/elisa5.pdf.
56 P. Mahanti, Arizona State University, Tempe, Arizona, 2008.
57 D. A. Gornall and S. N. L. Roth, *Clin. Biochem.*, 1996, **29**, 379–384.
58 J. P. Laurino, E. W. Bender, N. Kessimian, J. Chang, T. Pelletier and M. Usategui, *Clin. Chem.*, 1996, **42**, 1454–1459.
59 B. Beneteau-Burnat, B. Baudin and M. Vaubourdolle, *J. Clin. Lab. Anal.*, 2001, **15**, 314–318.
60 P. Mahanti, T. Taylor, D. Cochran, M. A. Hayes and M. M. Petkus, *Proceedings of SSC Asilomar*, 2008, **42**, 1975–1978.
61 U. Vovk, F. Pernus and B. Likar, *IEEE Trans. Med. Imaging*, 2007, **26**, 405–421.
62 F. Leong, M. Brady and J. O. McGee, *J. Clin. Pathol.*, 2003, **56**, 619–621.
63 J. Kittler and J. Illingworth, *Pattern Recognit.*, 1986, **19**, 41–47.